

## THICK DISKS IN THE HUBBLE SPACE TELESCOPE FRONTIER FIELDS

BRUCE G. ELMEGREEN<sup>1</sup>, DEBRA MELOY ELMEGREEN<sup>2</sup>, BRITTANY TOMPKINS<sup>2</sup>, LEAH G. JENKS<sup>2,3</sup>*Draft version November 13, 2018*

## ABSTRACT

Thick disk evolution is studied using edge-on galaxies in two Hubble Space Telescope Frontier Field Parallels. The galaxies were separated into 72 clumpy types and 35 spiral types with bulges. Perpendicular light profiles in F435W, F606W and F814W (B, V and I) passbands were measured at 1 pixel intervals along the major axes and fitted to  $\text{sech}^2$  functions convolved with the instrument line spread function (LSF). The LSF was determined from the average point spread function (PSF) of  $\sim 20$  stars in each passband and field, convolved with a line of uniform brightness to simulate disk blurring. A spread function for a clumpy disk was also used for comparison. The resulting scale heights were found to be proportional to galactic mass, with the average height for a  $10^{10 \pm 0.5} M_{\odot}$  galaxy at  $z = 2 \pm 0.5$  equal to  $0.63 \pm 0.24$  kpc. This value is probably the result of a blend between thin and thick disk components that cannot be resolved. Evidence for such two-component structure is present in an inverse correlation between height and midplane surface brightness. Models suggest that the thick disk is observed best between the clumps, and there the average scale height is  $1.06 \pm 0.43$  kpc for the same mass and redshift. A  $0.63 \pm 0.68$  mag V-I color differential with height is also evidence for a mixture of thin and thick components.

*Keywords:* galaxies: formation, galaxies: high-redshift, galaxies: spiral, galaxies: structure

## 1. INTRODUCTION

Thick disks are an old and faint component of most modern galaxies (Burstein et al. 1979; Gilmore & Reid 1983; Dalcanton & Bernstein 2002; Yoachim & Dalcanton 2006, 2008b; Comerón et al. 2011, 2014). They have high  $\alpha/Fe$  abundance ratios, indicating rapid formation, and they have low metallicities and red colors because they are old (e.g., Fuhrmann 1998; Bensby et al. 2007). They were much brighter in the early universe when they were young, as can be seen directly in Hubble Space Telescope deep fields where the angular resolution is typically comparable to the thick-disk scale height (Elmegreen & Elmegreen 2006).

Observations of the thick and thin disks in the Milky Way suggest that the transition from one to the other over time was relatively smooth. There is a continuous change in the distribution of stellar mass (Bovy et al. 2012a) and height (Bovy et al. 2012b) as stars change from the thick disk with high  $\alpha/Fe$  and low  $Fe/H$  to the thin disk. The distribution of stellar surface density as a function of scale height is also smooth, with a steady increase in surface density while the scale height decreases (Bovy et al. 2012a).

A sharper difference between Milky Way thick and thin disk stars is shown by the distribution of  $\alpha/Fe$  versus  $Fe/H$  for different intervals of height and galactocentric radius (Hayden et al. 2015). High  $\alpha/Fe$  stars show up primarily at heights  $z > 1 - 2$  kpc and radii  $R < 9$  kpc, while low  $\alpha/Fe$  stars occupy large heights,  $z > 1 - 2$  kpc, primarily in the outer disk,  $R > 9$  kpc, and low heights throughout the whole disk. There is also a dis-

tribution in the distribution of azimuthal speed,  $V_{\phi}$ , versus  $Fe/H$  (Lee et al. 2011): for the thin disk,  $V_{\phi}$  decreases with increasing  $Fe/H$  to values even larger than solar, reflecting the selection of inner-disk stars near the Sun at the outer parts of their epicycles and outer-disk stars near the Sun at the inner parts of their epicycles. On the other hand, for the thick disk,  $V_{\phi}$  increases with increasing  $Fe/H$ , up to and slightly overlapping with the lower limit on  $Fe/H$  for the thin disk, reflecting an increasing rotation speed for stars orbiting closer to the midplane. The latter is the effect of stellar pressure on orbit speed, i.e., asymmetric drift (Binney & Tremaine 2008). Liu & van de Ven (2012) also found that thick disk stars have higher eccentricities than thin disk stars, consistent with an early phase of scattering by massive clumps (Bournaud et al. 2009), although simulations of this process by Inoue & Saitoh (2014) did not reproduce the Milky Way's decrease in eccentricity for increasing metallicity.

The Milky Way thick disk is apparently shorter than the thin disk (Bovy et al. 2012c; Cheng et al. 2012; Bensby et al. 2011; Bensby 2017), reflecting inside-out growth from an increase in accreted angular momentum over time (Pichon et al. 2011). This change is reproduced in Milky Way simulations, where the disk scale length increases as the scale height decreases in a continuous fashion (Sánchez-Blázquez et al. 2009; Bird et al. 2013; Stinson et al. 2013; Aumer & White 2013; Martig et al. 2014; Minchev et al. 2015; Athanassoula et al. 2016). If a galaxy forms quickly, such as a massive disk galaxy (Behroozi et al. 2013), then both the thick (early-forming) and thin (late-forming) components can be old today, as observed by Comerón et al. (2016) and Kasparova et al. (2016). At the other extreme, dwarf irregular galaxies form slowly and are nearly pure thick disks today in terms of the ratio of height to radius (e.g., Elmegreen & Hunter 2015; Comerón et al. 2014). Because the star formation rate in galaxies depends on their

<sup>1</sup> IBM Research Division, T.J. Watson Research Center, 1101 Kitchawan Road, Yorktown Heights, NY 10598; bge@us.ibm.com

<sup>2</sup> Department of Physics & Astronomy, Vassar College, Poughkeepsie, NY 12604; elmegreen@vassar.edu

<sup>3</sup> Colgate University, Department of Physics and Astronomy, Hamilton, NY 13346

mass (Behroozi et al. 2013), galaxies more massive than the Milky Way should also have high  $\alpha/Fe$  in both their thick disks and the older parts of their thin disks. Disks less massive than the Milky Way should have low  $\alpha/Fe$  even in their thick parts.

Thick disks are expected for young galaxies because the turbulent speed in the gas is high compared to the rotation speed (Förster Schreiber et al. 2009; Kassin et al. 2012). Then stars that form in this gas will be relatively high-dispersion too. High turbulent speeds may result from rapid accretion, disk instabilities, and stellar feedback (Bournaud et al. 2009; Elmegreen & Burkert 2010; Martig et al. 2014; Forbes et al. 2014). Observations in support of this turbulent picture are in Robin et al. (2014); Aumer et al. (2016) show that stellar scattering from giant molecular clouds is not enough to make the thick disk. Thick disks can also form from thin disks that have a minor merger, but then the thick disks might be expected to flare and that is not observed (Bournaud et al. 2009; Comerón et al. 2011; Robin et al. 2014). Also with mergers, some examples should be seen with counter-rotation. Comerón et al. (2015) state that in the one case they observed, the thick disk rotates in the prograde direction, while Yoachim & Dalcanton (2008a) report a possible case with counter-rotation. Another model is that stellar migration in a thin disk gives the appearance of a thick disk component, but Vera-Ciro et al. (2014) and Vera-Ciro & D’Onghia (2016) suggest that migration affects only the thin disk.

This paper measures the disk thicknesses of galaxies in the HST Frontier Fields (Lotz et al. 2017) Abell 2744 Parallel and MACS J0416.1-2403 Parallel (hereafter, galaxies from these fields are abbreviated Axxxx and Mxxxx), which have tabulated redshifts and masses. The sample and instrument corrections are discussed in Section 2 and the results are in Section 3.

## 2. DATA AND METHODS

### 2.1. Sample Selection

Hubble Space Telescope archival data of two Frontier Fields were used for this study. The Frontier Fields are a set of deep images that consist of six galaxy clusters and six corresponding parallel fields. Abell 2744 and MACS J0416.1-2403 are the first fields that were catalogued and publicly available; here we examine their corresponding parallel fields. For our analysis we utilized images in the F435W, F606W and F814W filters, hereafter abbreviated as B, V and I. These were taken by the Hubble ACS camera and have an image depth of 140 orbits. The images are 10,800 x 10,800 pixels and have a scale of 0.03 arcsec pixel<sup>-1</sup>. Data on the fields were obtained from the AstroDeep Frontier Fields Catalogues, given by Castellano et al. (2016) and Merlin et al. (2016). These catalogues were compiled using multi-wavelength photometry and spectral energy distributions to determine redshifts and restframe galaxy properties. With IRAF (Image Reduction and Analysis Facility) and DS9, we identified by eye and classified all galaxies in the two fields that appeared to be linear and edge-on, resulting in a first sample of 188 galaxies.

Among the identified galaxies, 44 were excluded from further analysis due to several causes: faintness, a possible merger remnant, not edge-on or not straight, or

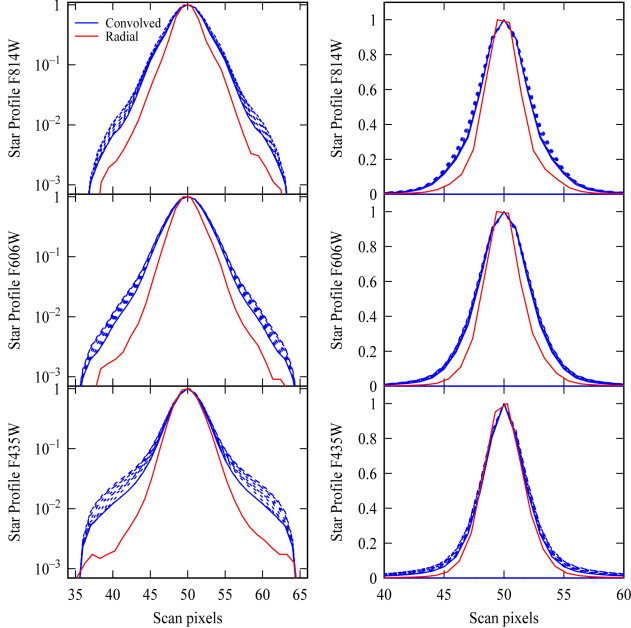
having redshifts  $\sim 0.01$  in the catalog, which is inconsistent with nearby high-redshift galaxies that look similar. The remaining 144 galaxies from both fields were analyzed. These had angular radii larger than 10 pixels (0.3 arcsec) and physical radii larger than  $\sim 2$  kpc. The outer reliable isophotes of the galaxies correspond to  $\sim 28$  mag arcsec<sup>-2</sup> in surface brightness. Most of the selected galaxies fall into the redshift range of  $z=0.5$  to 4.

Galaxies were first classified into spiral, clumpy, spheroidal and transition types using the images in DS9 and midplane light profiles from the task *pvector* in IRAF. The clumpy galaxies are characterized by distinct regions of star formation, visible as clumps in the images and as peaks in the radial profiles of these galaxies. Spiral galaxies were identified by a central bulge and an exponential radial profile. Transition galaxies did not fit cleanly into the clumpy or spiral categories based on their radial profiles, but often showed a bulge with a relatively large second clump. Spheroidal galaxies did not show observable clumps or exponential radial profiles, and had indistinct structure. Our sample had 72 clumpy galaxies, 35 spiral galaxies, 30 transition galaxies, and 7 spheroidal galaxies in the two fields combined. After further consideration, we eliminated the transition and spheroidal types as we could not be certain that the associated perpendicular intensity profiles were really sampling the thicknesses of the stellar distributions rather than a warp or tidal feature. Here we discuss the perpendicular profiles of the 72 clumpy galaxies and 35 spirals.

### 2.2. Point Spread Function for Image Deconvolution

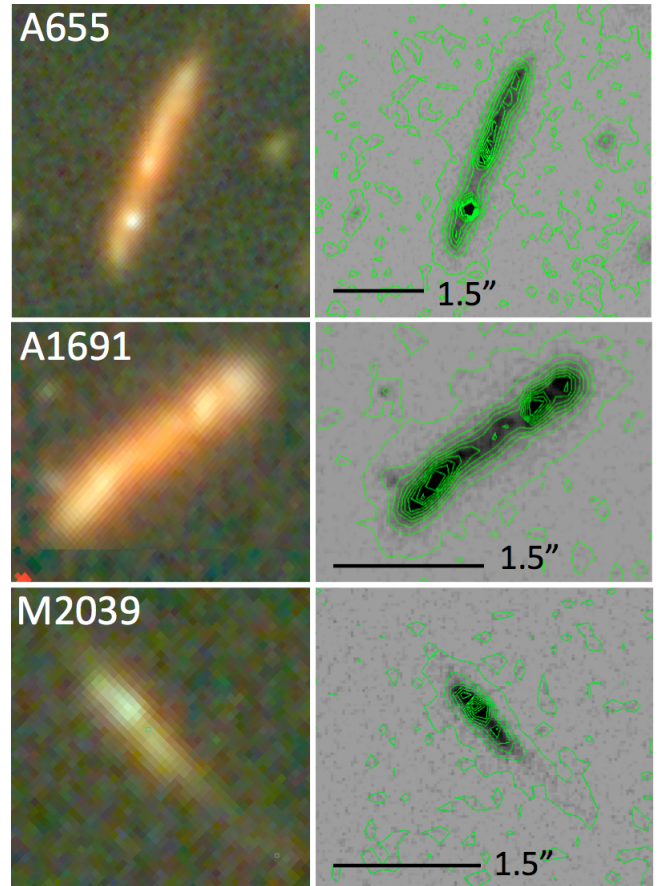
The point spread function of the instrument was evaluated by stacking approximately 20 stars in each field in B, V, and I passbands. Four scans spaced by equal angles through the stacked stellar images were then used to find the average stellar profiles. The stacked image looked relatively symmetric and the four scans were similar to each other.

Image deconvolution by a symmetric PSF depends on the shape of the imaged source. If the source is another star, then its deconvolution can be done using only the average linear scan through the PSF. However, if the source is an edge-on galaxy disk, then deconvolution can only be done with a “line spread function” (LSF), which is the convolution of the PSF with a line of infinitesimal thickness. The LSFs for each passband in field Abell 2744 are shown in Figure 1 (blue solid curves), along with the intensity scans through the stacked stars (red curves). The left-hand side uses a logarithmic scale to highlight the differences in the profile wings; the right-hand side shows the same profiles with a linear scale. The LSF is broader than the PSF below  $\sim 10\%$  of the peak because the PSF has broad non-Gaussian wings. If the PSF were point-symmetric and Gaussian, then the LSF would be the same as the PSF because integrations through a Gaussian in two orthogonal directions are independent. The profiles for the other field, MACS J0416.1-2403, are similar and not shown. See also Comerón et al. (2017) for a discussion of this modification to the PSF for edge-on galaxies. Sandin (2015) discusses possible problems in the measurement of thick disks because of improper removal of the PSF.



**Figure 1.** The average radial scans through stacked stellar images are shown as red curves for the three passbands of our observations. The convolutions of the two-dimensional stellar images with a line of brightness, the line spread functions (LSF), are shown as solid-line blue curves. The profiles are the same on the left and right, with the left using a log scale in the vertical direction to highlight the slight differences between the stellar images and the LSF at low intensities. Dotted blue curves use a clumpy LSF.

A clumpy line spread function (CLSF) was also made by convolving the stellar PSF with a line of brightness on which is superposed a uniformly bright region 6 pixels wide (the “clump”), which is the typical width of a large clump, and 6 times the line intensity, which is the typical brightness factor. The reason for doing this was to assess the effect of clumps on perpendicular scans through the interclump regions; some of that clump emission can contaminate the interclump scan because of its presence in the wings of the PSF. We found that when the bright part of the CLSF passes through the center of the PSF (as if the perpendicular intensity scan were going through a clump), the CLSF looks essentially the same as the LSF because both the clump and the line are dominated by the sharp central part of the PSF peak. When the bright part of the CLSF is far from the center of the PSF, the CLSF is again the same as the LSF because the PSF is too weak at this distance to pick up the clump. At intermediate distances, the bright part adds to the wings of the CLSF and makes it a little broader than the pure LSF. The blue dotted curves in Figure 1 show these CLSF for clump central positions starting at 3 pixels from the peak of the PSF and with uniform pixel spacings up to 13 pixels from the peak. The excess over the LSF increases with distance at first and then decreases. The maximum excess for the F814W passband occurs around 8 pixels from the PSF center (Fig. 1) and equals a factor of 3.6 for a clump center that is 4 to 5 pixels from the center. This excess factor does not affect the results much (see below) because it is in a part of the LSF that is already down from the peak by a factor of  $\sim 100$ .



**Figure 2.** Three clumpy galaxies are shown in color on the left using F435W, F814W, and F160W filters. Contours for the same galaxies are shown on the right using contour values ranging from 0 to 0.01 counts in steps of 0.001 counts. The contours at the apparent edge of the optical image are around  $3\sigma$ .

### 3. RESULTS

#### 3.1. Scale Height Determination and an anti-correlation with Intensity

Figures 2 and 3 show three clumpy galaxies and three spiral galaxies along with their surface brightness contours. Intensity contours are from 0 to 0.01 counts in steps of 0.001 counts. The contours at the apparent edge of the optical image are  $3\sigma$ . These  $3\sigma$  contours are fairly straight around the clumpy galaxies, and they are bowed-out around the bulge regions of the spiral galaxies. We discuss in Section 3.2 the implication of this observation, which is that the perpendicular scale height tends to decrease near the clumps in clumpy galaxies, while it is more constant throughout the bulge and disk of spiral galaxies. First, this trend will be shown for all of the galaxies here.

Figure 4 shows perpendicular I-band intensity profiles in steps of 5 pixels along the major axis of A1691, which is the middle galaxy in Figure 2. The intensity, measured in image counts $\times 1000$ , peaks at the center of each scan, which is the midplane of the disk. The peaks are higher near the ends of the galaxy because of bright clumps (Fig. 2). The scan near the center of the galaxy, which is pixel number 40, is shown as a dashed line.

Perpendicular intensity scans like these were measured for each galaxy and passband and spaced by single pixel

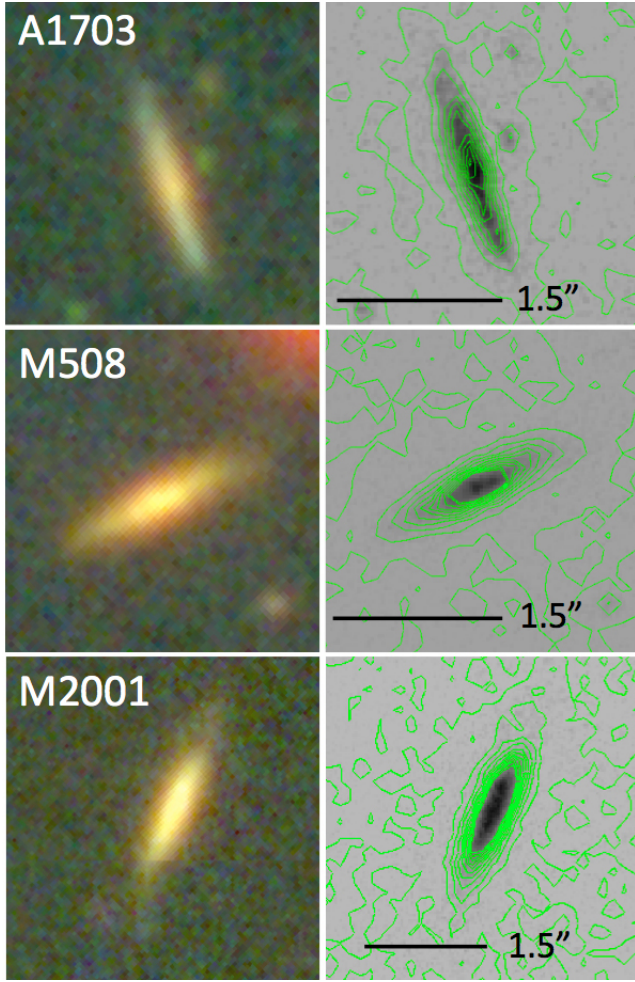


**Figure 3.** Three spiral galaxies are shown in color on the left using F435W, F814W, and F160W filters. Contours are on the right ranging from 0 to 0.01 counts in steps of 0.001 counts.

increments along the major axes. The scans were fitted to  $\text{sech}^2$  functions that were blurred by the line spread function, LSF, discussed in Section 2. To be specific, the fitting minimized the rms difference between a blurred  $\text{sech}^2([i - i_0]/H)$  function of the pixel number,  $i$ , and the intensity scan normalized to unit height,  $I_{\text{norm}}(i)$ , with fitting parameters equal to the width of the model function,  $H$ , also in pixels. In other words, we determined the function

$$\text{sech}^2([i - i_0]/H) = \left( \frac{2}{e^{(i-i_0)/H} + e^{-(i-i_0)/H}} \right)^2 \quad (1)$$

such that the convolution,  $C(i)$ , of  $\text{sech}^2$  with the LSF,  $L(i)$ , i.e.,

$$C(i) = \sum_{i'=-\infty}^{\infty} L(i - i') \text{sech}^2([i' - i_0]/H) di' \quad (2)$$

has the smallest rms compared to the observations,  $I_{\text{norm}}(i)$ , when  $C(i)$  is also normalized,

$$\text{rms}^2 = \sum_{i=-\infty}^{\infty} (I_{\text{norm}}[i] - C_{\text{norm}}[i])^2 di. \quad (3)$$

This fitting was done numerically by iteration.

Figure 5 shows a typical result from the perpendicular profile at position 40 in the galaxy A1691, which is the

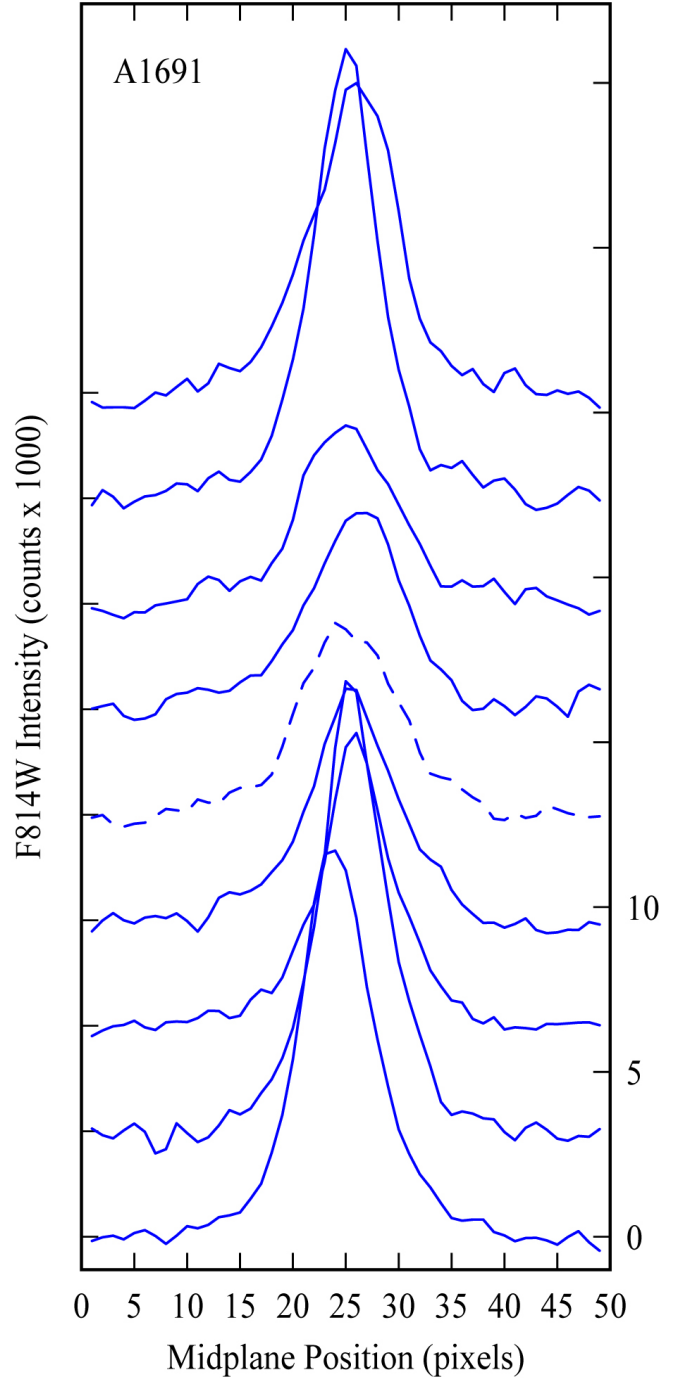
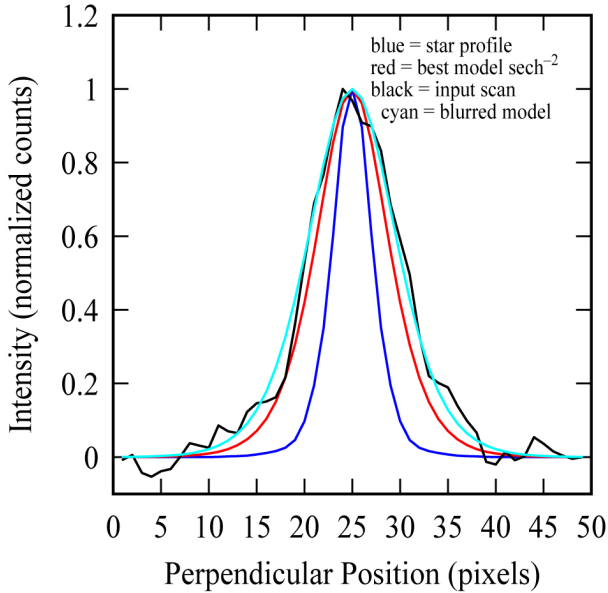


**Figure 4.** Intensity scans perpendicular to the disk of the clumpy galaxy A1691 taken every 5 pixels along the midplane. The central scan at pixel number 40 is indicated by a dashed line.

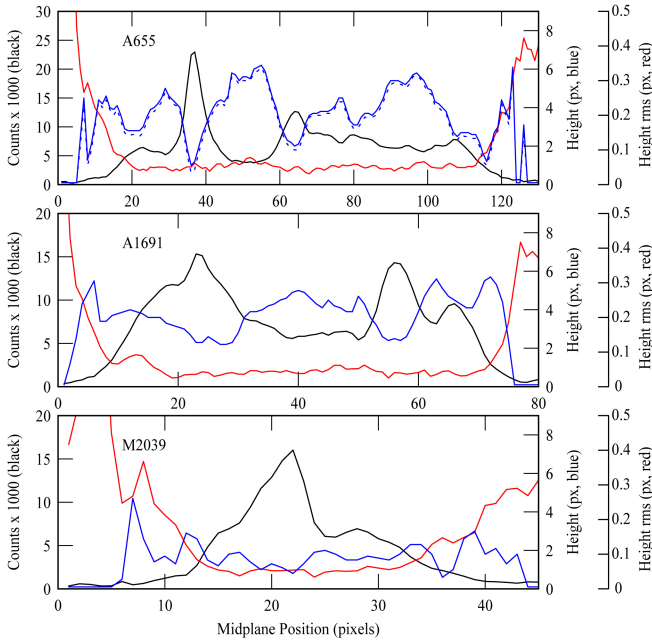
dashed profile in Figure 4. The black curve is the measured profile (“input scan” in the figure label). The blue curve is the stellar LSF, the red curve is the fitted  $\text{sech}^2$  function, and the cyan curve is the LSF-blurred  $\text{sech}^2$  function, which is the best match to the observations. All of the profiles have been normalized to unit height. In this case,  $H = 5.0$  pixels and the rms deviation for the fit is 0.038 counts.

Figure 6 shows for the three clumpy galaxies in Figure 2: the midplane intensity as a function of position





**Figure 5.** Sample F814W profile through the center of the clumpy galaxy A1691 (black curve) with the best-fit, LSF-convolved profile shown in cyan, along with the intrinsic disk profile before convolution with the LSF in red, and the stellar LSF in blue.



**Figure 6.** Results for the three clumpy galaxies in Figure 2. In each panel, the black curve shows the midplane F814W intensity measured along the major axis of the galaxy, the blue curve shows the fitted scale height for each major axis position, and the red curve shows the rms error between the fitted solution and the observed scan. In the main part of the disk, there is an anti-correlation between the midplane intensity and the fitted height that is modeled in Section 3.2 as the result of a superposition of a thick and a thin disk component with variable relative intensities. The dotted blue curve for A655 shows the fitted scale heights when a clumpy line spread function is used to deconvolve the vertical profiles.

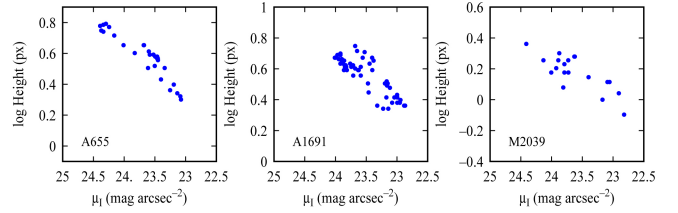


**Figure 7.** The fitted scale heights,  $H$ , are plotted versus the midplane intensities measured in magnitudes  $\text{arcsec}^{-2}$  in the I band for the three clumpy galaxies in Figure 2. The anti-correlation between the height and the intensity is clear for these galaxies.

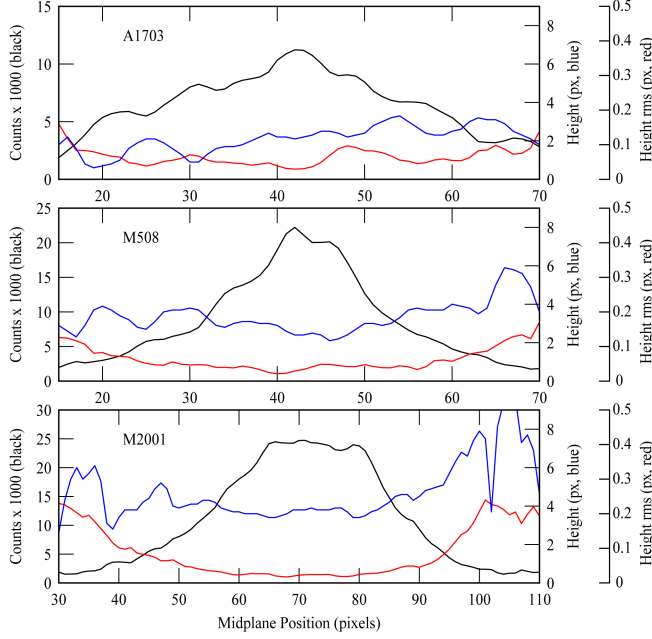
along the midplane (black curves), the fitted height from perpendicular scans, also as a function of midplane position (blue curves), and the rms between the fitted  $\text{sech}^2$  function and the perpendicular scan (red curves). The clumpy structure in these galaxies can be matched to the peaks and valleys in the intensity scans. The scale for intensity is counts  $\times 1000$  as indicated on the left-hand axis. The scales for height and rms in pixels are on the right-hand axes. In the figure, the scale heights,  $H$ , range from  $\sim 2$  pixels for M2039, to  $\sim 4$  pixels for A1691, to  $\sim 6$  pixels for A655.

The top left panel of Figure 6 has a dotted blue curve that is the solution to the scale height when the clumpy line spread function (CLSF) is used (cf. Sect. 2.2). The model clump in the CLSF has a uniform brightness between 5 and 11 pixels from the center of the PSF and an amplitude 6 times the brightness of the line intensity. These were the parameters that gave the maximum deviation between the CLSF and the LSF in Section 2.2. The dotted curve shows that the fitted scale height decreases by only  $\sim 1\%$  for deconvolution with the CLSF compared to the LSF. This is a small change because the spacings between the main clumps are usually well resolved by the PSF.

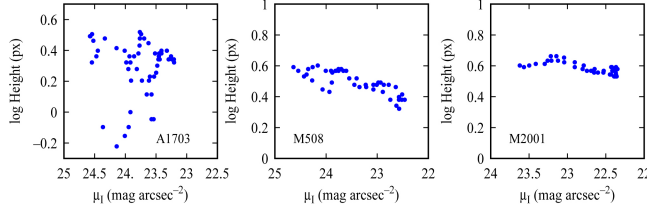
Figure 6 reveals a pattern where regions of high intensity correspond to relatively low scale heights, and vice versa. This pattern is shown better in Figure 7, which plots, for the same three galaxies, the log of the height in pixels versus the I-band surface brightness,  $\mu_I$ , in magnitudes per  $\text{arcsec}^2$ . The correlation has slopes of  $d \log H / d \mu_I = 0.32 \pm 0.04$ ,  $0.28 \pm 0.04$ , and  $0.21 \pm 0.06$  for A655, A1691, and M2039, respectively. Converting these magnitudes to intensity counts,  $C_I$ , the slopes are  $d \log H / d \log C_I = -0.79 \pm 0.10$ ,  $-0.70 \pm 0.11$ , and  $-0.53 \pm 0.16$ , respectively. The uncertainties in the slopes were determined from the Student-t distribution.

Figure 8 shows the same midplane scans and fits for the three spiral galaxies in Figure 3, and Figure 9 shows the heights versus the midplane surface brightnesses for these galaxies. The anti-correlation is not as strong for spirals as it is for the clumpy types.

Height-intensity anti-correlations like this were fitted for all of the galaxies in our sample using plots of the log of the height in pixels versus the log of the intensity in counts. Figure 10 shows histograms of the slopes in these anti-correlations. The bottom histogram is for the spiral and clumpy galaxies combined, the middle histogram is for the spirals, and the top histogram is for the clumpy galaxies. The average slope for the all of the galaxies is  $< d \log H / d \log C_I > = -0.38 \pm 0.73$ ; for the clumpy galaxies it is  $-0.47 \pm 0.84$ , and for the spirals it is  $-0.17 \pm 0.30$ . The spirals have a significantly weaker height-intensity



**Figure 8.** Results for the three spiral galaxies in Figure 3. Black curves are the midplane intensities, blue curves are the fitted scale heights, and red curves are the rms errors, as in Figure 6. There is very little anti-correlation between the midplane intensity and the fitted height for spiral galaxies because the thin and thick disks are both highly evolved.



**Figure 9.** The fitted scale heights,  $H$ , are plotted versus the midplane intensities measured in magnitudes  $\text{arcsec}^{-2}$  in the I band for the three spiral galaxies in Figure 3.

anti-correlation than the clumpy galaxies.

An example of this difference between galaxies that have an anti-correlation and those that do not is shown in Figures 11 and 12. The left-hand panel of Figure 12 has two perpendicular intensity scans for a clumpy galaxy (galaxy A655 in Fig. 2), one from a bright clump and another from a faint interclump region shown as solid curves, and the right-hand panel has two perpendicular intensity scans for a spiral galaxy (galaxy A1703 in Fig. 3), one from the bulge and another from the disk. The regions chosen are shown in Figure 11. In each panel of Figure 12, the dashed red curve is the same as the solid red curve but stretched upward to match the peak of the solid blue curve. For the clumpy galaxy, the bright region with the higher peak (blue curve) is clearly narrower than the faint region (red curve), while for the spiral galaxy, both regions have about the same profile widths.

This difference in height-intensity correlation for spiral and clumpy galaxies is also evident directly from the contours in Figure 2, as mentioned previously. The contours around the clumpy galaxies are fairly straight on each side of the clumps, whereas the contours bow out to a V-shape around the bright parts of the spiral. For

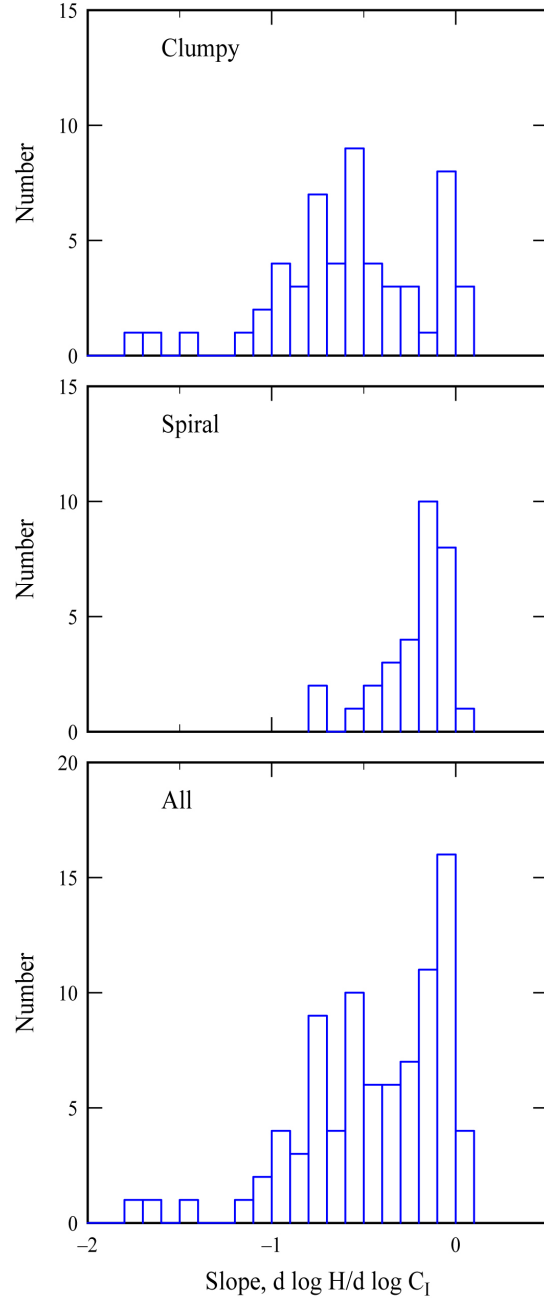


**Figure 10.** Histograms are shown for the slope of the anti-correlation between the fitted scale height and the midplane intensity. The scale height is  $H$  and the I-band intensity measured in counts is  $C_I$ . The strong anti-correlation for the clumpy galaxies shows up here as a significant shift to negative values for the correlation slope. The shift is less for spiral galaxies.

the clumpy galaxies, the straight contours mean that the intensity at a certain height above the midplane is independent of the intensity in the midplane, and for this to be true, the scale height has to be smaller in the regions of higher intensity. For the spirals, the greater intensity at fixed height above the brighter regions corresponds to an increase in the intensity of the whole vertical profile with an approximately fixed profile width.

### 3.2. Model for the anti-correlation

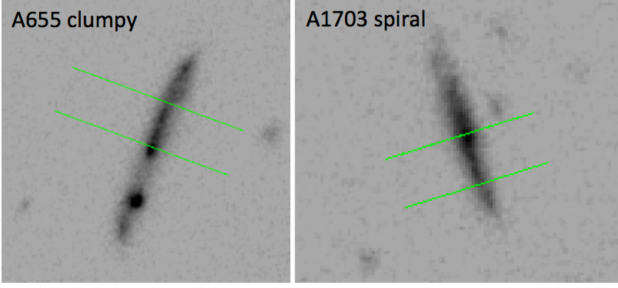


**Figure 11.** Two galaxies from Figures 2 and 3 with perpendicular cut positions used to illustrate the difference between perpendicular profiles in Figure 12.

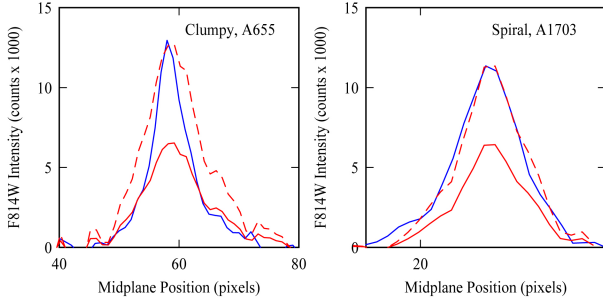


**Figure 12.** Perpendicular intensity profiles for the cuts indicated in Figure 11 showing how the clump profiles are thinner when they are higher, but the spiral profiles are about the same width. The raw profiles are plotted as solid curves with the stronger profile in blue. The dashed red curve is the same as the solid red curve but multiplied by a constant factor to give the same peak.

The anti-correlation for clumpy galaxies, and the average value of its slope,  $-0.47 \pm 0.84$ , make sense if there are two components in each galaxy, a bright thin disk and a faint thick disk, which blend together into our single  $\text{sech}^2$  fitting function at the relatively poor resolution of the survey. Consider what happens as the thin component gets brighter. Let  $A_{\text{thin}} \exp(-z/H_{\text{thin}})$  be an approximation for the thin component at  $z > H_{\text{thin}}$  and let  $A_{\text{thick}} \exp(-z/H_{\text{thick}})$  be an approximation for the thick component off the midplane. When the thin component is faint, the profile is dominated by the thick component and the measured thickness is  $H_{\text{thick}}$ . This remains true until the brightness of the thin component at a height equal to the scale height of the thick component becomes equal to the brightness of the thick component there,

$$A_{\text{thin}} e^{-H_{\text{thick}}/H_{\text{thin}}} \sim A_{\text{thick}} e^{-1}. \quad (4)$$

Then the main part of the thick disk is dominated in brightness by the thin component and the measured scale height is the thin component value. Thus there is a transition from the thick component scale height to the thin component scale height as the thin component brightness increases from zero to

$$A_{\text{thin}} = A_{\text{thick}} e^{(H_{\text{thick}}/H_{\text{thin}} - 1)}. \quad (5)$$

The logarithmic derivative corresponding to this transition is approximately

$$\frac{d \log H}{d \log A} \sim -\frac{\ln(H_{\text{thick}}/H_{\text{thin}})}{H_{\text{thick}}/H_{\text{thin}} - 1}. \quad (6)$$

For  $H_{\text{thick}}/H_{\text{thin}}$  equal to typical values of 3 to 5 (Comerón et al. 2011), this logarithmic derivative ranges

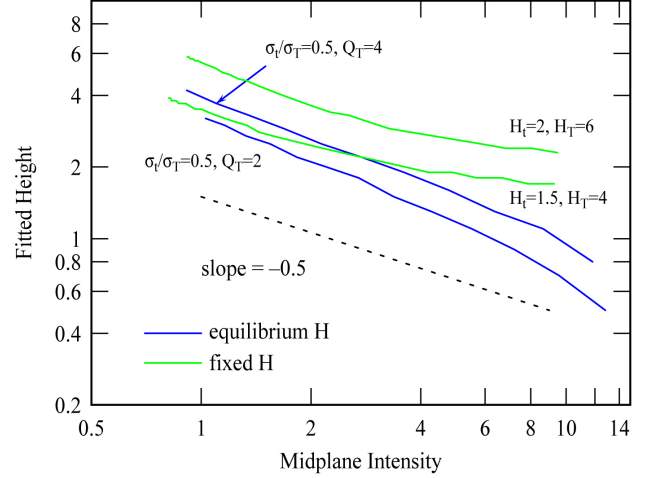


**Figure 13.** Two models for the anti-correlation between the height that is determined by fitting a two-component disk with a single  $\text{sech}^2$  function and the midplane intensity. The green curves have fixed scale heights for the two components and a variable intensity for the thin component, while the blue curves have two components in vertical equilibrium with a variable mass for the thin component. Both models have a slope of about  $-0.5$ , which is what we observe for the clumpy galaxies. The midplane intensity is from the sum of the two components, as would be observed for a real galaxy.

between  $-0.55$  and  $-0.40$ , as observed in Figure 10.

Two detailed models for this anti-correlation were also considered. The first makes a two component disk with fixed scale heights for each component and a fixed central brightness for the thick component. Then it varies the central brightness of the thin component, blurs the combined disk with our LSF, and stores the result as a mock observation. This observation is then fed into our main deconvolution program to recover the input disk as fitted by a single  $\text{sech}^2$  function. The resulting thickness of the fitted composite disk is plotted versus the total measured intensity of the midplane (from the blurred sum of the thin and thick disks) as a green line in Figure 13 for two cases, one with  $H_{\text{thin}} = 2$  and  $H_{\text{thick}} = 6$ , and another with  $H_{\text{thin}} = 1.5$  and  $H_{\text{thick}} = 4$ . Both have fitted heights at low intensity that are about equal to the thick disk scale height, and fitted heights at high intensity that are about equal to the thin disk scale height. The anti-correlation has a slope of  $\sim -0.5$ , as shown by the fiducial dotted line. This is similar to what we observe in the real galaxies.

The second model makes a two-component disk that is in hydrostatic equilibrium following equations in Narayan & Jog (2002), but without the dark matter component. We assume a ratio of velocity dispersions for the thin and thick disks equal to 0.5, a Toomre- $Q$  value for the thick disk equal to 2 and 4 in two cases, and a variable ratio of the surface density of thin disk to thick disk. As the thin disk component increases in mass relative to the thick disk, the thick disk scale height decreases because of the larger gravitational attraction to the midplane. Thus there are two effects causing an anti-correlation in this case. The results are shown as blue curves in Figure 13. The slope is also about  $-0.5$ .

The anti-correlation slope for the model with fixed scale heights is about the same as the slope for the hydrostatic model with variable scale heights because the

brightening effect of the thin disk dominates the correlation in both cases. The shrinking thick disk in the equilibrium case cannot be seen beneath the brightening of the thin disk. If the thin disk were darker, adding mass but not light, or if the thick disk could be observed further from the midplane where the thin disk is very weak, then the shrinking of the thick disk with increasing thin disk mass should be observable. This is evidently an observation well suited for the James Webb Space Telescope, with its heightened sensitivity in the near-infrared.

An anti-correlation between scale height and midplane surface brightness should be expected in gas-dominated galaxies because star formation in the relatively thin component can be much brighter than the older stars in the thick component. A more evolved galaxy with less star formation should have less of an anti-correlation because the thin disk is less prominent compared to the thick disk. Presumably this is why the spiral galaxies in our survey have only weak anti-correlations between scale height and midplane surface brightness (Fig. 10). Spiral galaxies are more evolved than clumpy galaxies (Elmegreen & Elmegreen 2014).

### 3.3. Color Differentials over Height

The scale heights were measured for all three filters, B, V and I, but the B images were faint and had the largest rms values for the fits. Here we compare the V and I scale heights to search for vertical color gradients. The V band intensity at one scale height in the I band is

$$I_V = I_{V,0} \left( \frac{2}{e^{H_I/H_V} + e^{-H_I/H_V}} \right)^2, \quad (7)$$

and the I band intensity at one scale height in the I band is

$$I_I = I_{I,0} \left( \frac{2}{e^1 + e^{-1}} \right)^2. \quad (8)$$

The  $V - I$  color differential from the midplane to one scale height in I band is

$$\Delta(V - I) = (V - I)_{H_I} - (V - I)_0 = -5 \log \left( \frac{e^1 + e^{-1}}{e^X + e^{-X}} \right) \quad (9)$$

where  $X = H_I/H_V$ .

The distribution functions for  $\Delta(V - I)$  among all the galaxies are shown in Figure 14, divided into galaxy type. Although the distribution functions are broad, there is a slight offset toward redder  $V - I$  at one I-band scale height compared to the midplane. The average  $V - I$  reddenings are  $0.63 \pm 0.68$ ,  $0.89 \pm 0.76$ , and  $0.48 \pm 0.59$  for all galaxies, spirals, and clumpy galaxies, respectively.

Reddening of the starlight with distance from the midplane is another indication that there is a range of stellar populations including a thin young component and a thick old component. The corresponding age difference for a given reddening value depends on the redshift because of bandshifting. Figure 15 shows the  $V - I$  color differences at the I band scale height as a function of redshift with different symbols representing different mass ranges,  $10^7 - 10^8 M_\odot$ ,  $10^8 - 10^9 M_\odot$ ,  $10^9 - 10^{10} M_\odot$ , and  $10^{10} - 10^{11} M_\odot$ . The galaxies are divided into spiral

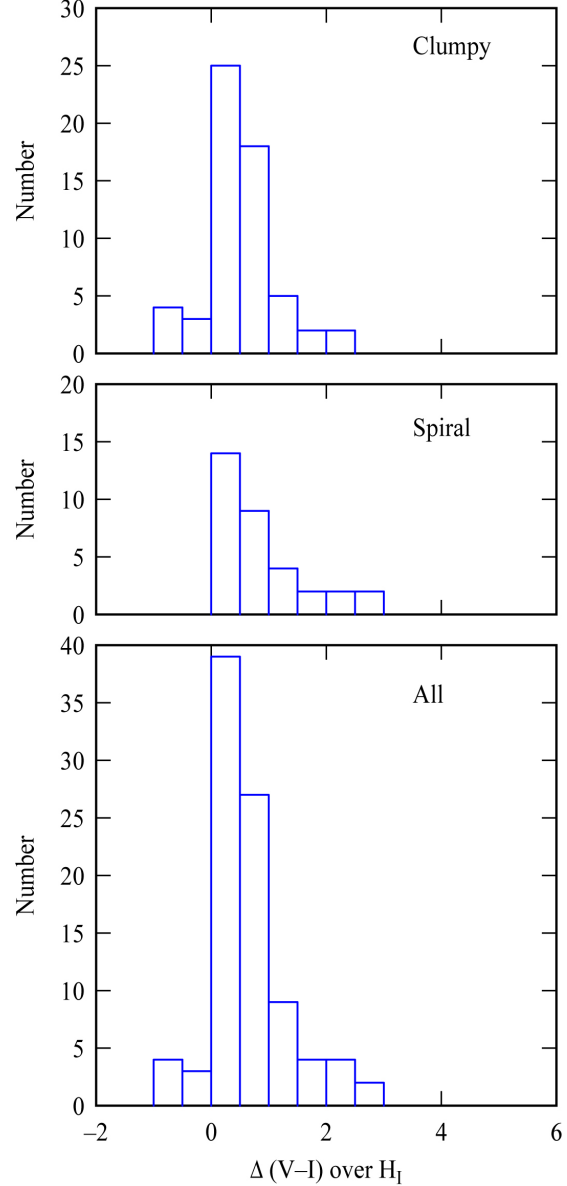


**Figure 14.** Histogram of the color differences between the midplanes of the galaxies and the positions at one scale height in I band above the midplanes.

and clumpy types. The spirals only occur at low redshifts, less than  $\sim 1.5$ , as found previously (Elmegreen & Elmegreen 2014), whereas the clumpy types extend to higher redshifts.

The curves on the panel for the clumpy galaxies in Figure 15 are models using Bruzual & Charlot (2003) stellar population spectra that were redshifted and integrated over the HST ACS filters used here. They include absorption from the intervening Lyman  $\alpha$  forest (Madau 1995) but no dust absorption (dust absorption in the thin disk component decreases the thick-minus-thin disk color difference, possibly making it negative). The different curves are for different values of  $\tau$  in a star formation history that is modeled as

$$\text{SFR}_{\text{thick}} = Ae^{-t/\tau} ; \quad \text{SFR}_{\text{thin}} = B(1 - e^{-t/\tau}). \quad (10)$$

These formulae assume the thick disk forms first with



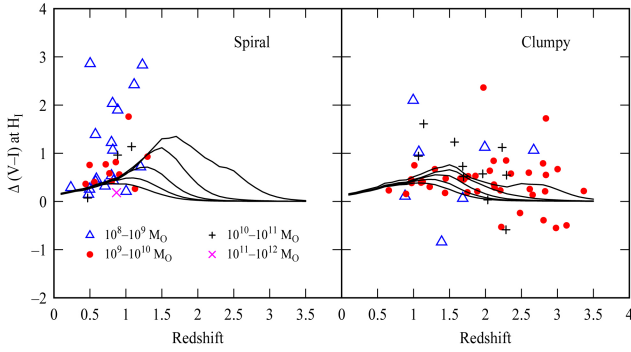


**Figure 15.** The color differences between the midplane and one scale height in I band are plotted versus the redshifts for different mass ranges indicated by different symbols. The curves are models based on star formation and stellar evolution in the thick and thin disk components. On the right, the curves have decay times,  $\tau$  in equation 11, that increase from 0.2 Gyr for the upper curve to 1 Gyr for the lower curve. The model assumes that the final thick disk mass equals the final thin disk mass. The curves are a reasonable fit to the red dots, which have an intermediate mass, as indicated on the left. The curves on the left have the same range of  $\tau$  but assume that the final thick disk mass is 3 times the final thin disk mass. They reach higher color differences but are not an ideal fit to the data.

an exponentially decaying rate, and the thin disk forms second with an exponentially increasing rate to a constant value. The coefficients  $A$  and  $B$  determine the relative star formation rates and therefore the relative final masses in the two components. Because what we need for comparison with the observations is the color gradient, we choose  $B = 1$  and

$$A = \frac{T - \tau(1 - e^{-T/\tau})}{\tau(1 - e^{-T/\tau})}, \quad (11)$$

which gives the thick and thin disk an equal mass after a Hubble time,  $T$ . The assumed values of  $\tau$  are 0.2 Gyr, 0.4 Gyr, up to 1 Gyr, in equal steps. Figure 15 shows a reasonable agreement between the model and the observations of clumpy galaxies in the mass range from  $10^9 - 10^{10} M_\odot$ . The low-mass spiral galaxies (on the left in Figure 15) have higher color differentials that we were not able to reproduce with this method. The curves in the left panel assume that the final thick disk mass is three times more than the final thin disk mass. This increases the color difference. Larger or smaller mass thick disks do not have even higher color differentials because in the first case the midplane starts to take on the color of the thick disk, decreasing the differential compared to the color at one scale height, and in the second case the disk at one scale height becomes dominated by the thin disk component, decreasing the color differential again.

#### 4. CORRELATIONS WITH GALAXY MASS AND REDSHIFT

Figure 16 shows the fitted scale heights in I-band converted to physical sizes in kpc using redshifts from Castellano et al. (2016), plotted versus the galaxy redshifts with different symbols representing different intervals of galaxy mass. The black dots represent the size of a single pixel at the redshift of a corresponding galaxy. The bottom two panels plot the average height in each galaxy, averaged over all of the pixels along the major axis where there is a good fit with a low rms. These

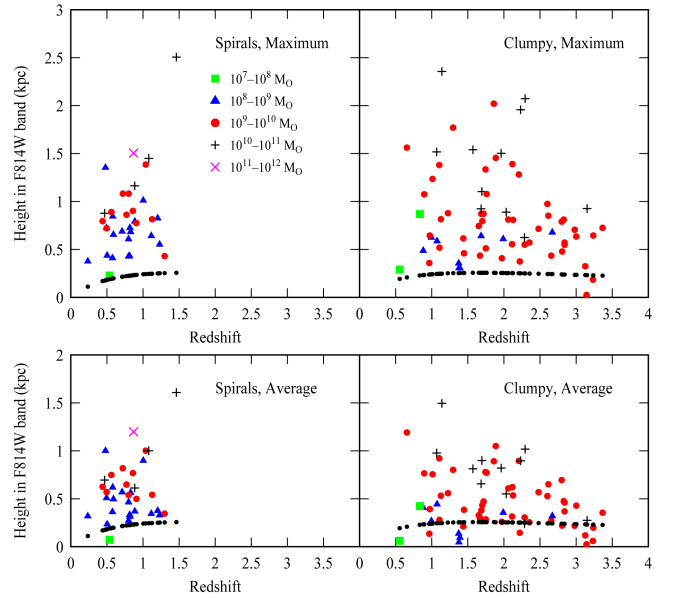
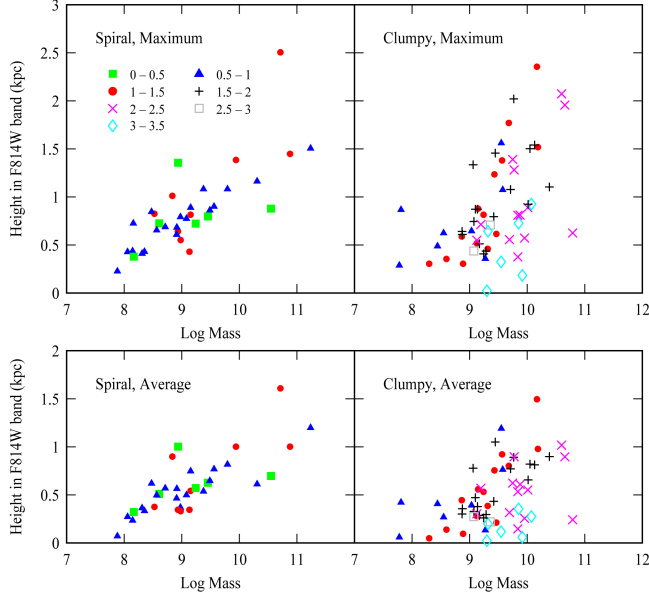


**Figure 16.** The scale heights in I band are shown versus the redshifts for spiral galaxies on the left and clumpy galaxies on the right. Galaxy mass ranges are indicated by the different symbols. The black dots at the bottom of each panel are the sizes of a single pixel at that redshift (one dot per galaxy). The top panels are the maximum heights measured for each galaxy, considered to be representative of the thick disk unblended with the thin disk, while the lower panels are the average heights for all of the single-component fits in each galaxy.

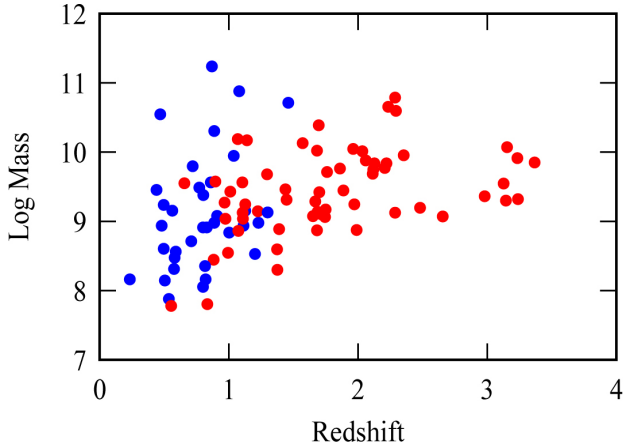
good-fit regions were determined for each galaxy by eye using plots like Figure 6. Typically, a range of pixels on each side of the nucleus was selected for the spiral galaxies in order to avoid the bulge. For the clumpy galaxies, the selected region usually extended through the whole disk. This averaging procedure means that the plotted values are between the high and low values of the fitted heights in the anti-correlation discussed in Section 3.1. To get a value more representative of the thick disk, the top panels plot the maximum height from all of the fitted values in the same pixel range. This maximum usually occurs where the midplane intensity is small. According to the models in Section 3.2, it should represent the thick disk scale height better than the average.

Figure 16 suggests that the thickest clumpy galaxies in the mass range  $10^9 - 10^{10} M_\odot$  (red points) tend to get thicker at decreasing redshift. That is, the top of the distribution of red points increases toward decreasing redshift. The thickest clumpy galaxies are also thicker than the spiral galaxies at the same redshift. To be specific, we determined average heights and maximum heights for clumpy galaxies with masses between  $10^{9.5}$  and  $10^{10.5}$  and for three redshift bins: 0.5-1.5, 1.5-2.5, and 2.5-3.5. The average heights in kpc are, respectively,  $1.03 \pm 0.25$ ,  $0.63 \pm 0.24$  and  $0.32 \pm 0.21$ . The maximum heights are  $1.61 \pm 0.39$ ,  $1.06 \pm 0.43$ , and  $0.60 \pm 0.27$ . In comparison, spiral galaxies in the same mass range and for redshifts between 0.5 and 1.5 have an average height of  $0.80 \pm 0.14$  and a maximum height of  $1.13 \pm 0.17$ .

This redshift correlation is probably the result of a mass correlation shown in Figure 17, which plots the average and maximum thicknesses for spiral and clumpy types as a function of mass with different symbols representing different redshift ranges, as indicated in the top



**Figure 17.** The height in I band is shown versus the galaxy mass with different symbols representing different redshift ranges as indicated in the left-hand panel. Spirals are on the left and clumpy galaxies are on the right. The maximum heights for each galaxy are in the top panels and the average heights for each galaxy are in the bottom panels.



**Figure 18.** Galaxy mass versus redshift with blue points for the spirals and red points for the clumpy galaxies.

left panel. There is a clear correlation between height and mass for all redshifts. Because the upper range of mass increases with decreasing redshift (Fig. 18), the height-mass correlation probably explains the height-redshift correlation in Figure 16.

Figure 19 shows the ratio of the average scale height for each galaxy to the galaxy radius determined from the extent of the disk in the I-band, down to about the  $3\sigma$  contour. Different symbols are for different redshift ranges. The upper limit to this ratio increases with mass but is approximately the same for spiral and clumpy types and independent of redshift.

## 5. CONCLUSIONS

The vertical scale heights of edge-on spiral and clumpy galaxies in two HST Frontier Field Parallels were measured after deconvolution from the instrument point

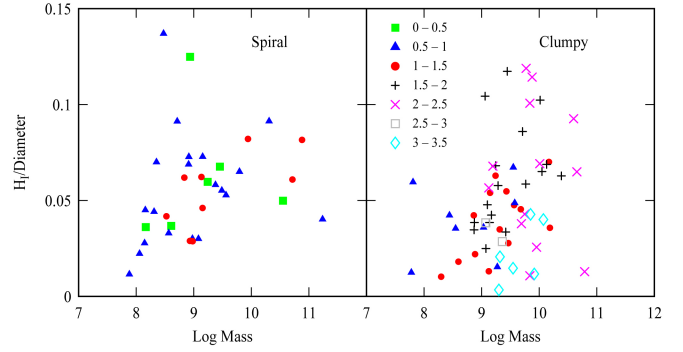


**Figure 19.** The ratio of disk height to disk diameter versus galaxy mass with different symbols representing different redshifts, as indicated in the right-hand panel.

spread function. The scale heights anti-correlate with midplane brightness for the clumpy galaxies, suggesting two components, a bright thin disk and a faint thick disk, with variations in the relative brightnesses of these components as a result of clumpy midplane star formation. Three models reproduced this anticorrelation. The vertical profiles also reddened slightly with height, suggesting the same two components with a difference in their formation times equal to a fraction of a Gyr. The scale heights increase with galaxy mass for both galaxy types and for all observed redshifts.

The observations indicate that clumpy galaxies have thick disks with somewhat thinner star formation components at redshifts out to at least  $z = 3$ . Spiral galaxies also have thick disks out to  $z \sim 1.5$ , as measured directly, but the anti-correlation between height and brightness is weaker than for clumpy types. This is presumably because the thin disk is older and the star formation bursts are weaker for spirals than clumpy types, and therefore the spiral thin disk has less contrast to its old thick disk.

*Acknowledgments* We gratefully acknowledge the National Science Foundation Grant AST-1005024 to the Keck Northeast Astronomy Consortium REU Program and the Vassar College Undergraduate Research Summer Institute. We thank the referee for useful comments.

## REFERENCES

- Athanassoula, E., Rodionov, S. A., Peschken, N., Lambert, J.C. 2016, *ApJ*, 821, 90  
Aumer, M. & White, S.D.M. 2013, *MNRAS*, 428, 1055  
Aumer, M., Binney, J., & Schönrich, R. 2016, *MNRAS*, 459, 3326  
Bensby, T., Zenn, A. R., Oey, M. S., & Feltzing, S. 2007, *ApJ*, 663, L13  
Bensby, T., Alves-Brito, A., Oey, M. S., Yong, D., & Meléndez, J., 2011, *ApJ*, 735, L46  
Bensby, T. 2017, *IAU Symposium* 321, Cambridge University Press: Cambridge, p.3  
Binney, J., & Tremaine, S. 2008, *Galactic Dynamics*, Princeton University Press  
Bird, J.C., Kazantzidis, S., Weinberg, D.H., Guedes, J., Callegari, S., Mayer, L., Madau, P. 2013, *ApJ*, 773, 43  
Bovy, J., Rix, H.-W., Hogg, D.W., Beers, T.C., Lee, Y.S., Zhang, L. 2012a, *ApJ*, 755, 115  
Bovy, J., Rix, H.-W., Liu, C., Hogg, D., W., Beers, T.C., Lee, Y.S. 2012b, *ApJ*, 753, 148  
Bovy, J., Rix, H.-W., Hogg, D.W. 2012c, *ApJ*, 751, 131  
Bruzual, G., & Charlot, S. 2003, *MNRAS*, 344, 1000  
Burstein, D. 1979, *ApJ*, 234, 829  
Behroozi, P.S., Wechsler, R.H., & Conroy, C. 2013, *ApJ*, 770, 57  
Bournaud, F., Elmegreen, B.G., & Martig, M. 2009, *ApJL*, 707, L1  
Castellano, M., Amorn, R., Merlin, E. et al. 2016, *A&A*, 590, A31  
Cheng, J.Y., Rockosi, C.M., Morrison, H.L., et al. 2012, *ApJ*, 752, 51

- Comerón, S., Elmegreen, B. G., Knapen, J. H., et al. 2011, *ApJ*, 741, 28
- Comerón, S., Elmegreen, B. G., Salo, H., et al. 2014, *A&A*, 571, A58
- Comerón, S., Salo, H., Janz, J., Laurikainen, E., Yoachim, P. 2015, *A&A*, 584, A34
- Comerón, S., Salo, H., Peletier, R. F., Mentz, J. 2016, *A&A*, 593, L6
- Comerón, S., Salo, H., Knapen, J. 2017, submitted
- Dalcanton, J. J., & Bernstein, R. A. 2002, *AJ*, 124, 1328
- Elmegreen, B. G. & Elmegreen, D. M. 2006, *ApJ*, 650, 644
- Elmegreen, B.G., & Burkert, A. 2010, *ApJ*, 712, 294
- Elmegreen, D. M., & Elmegreen, B. G. 2014, *ApJ*, 781, 11
- Elmegreen, B.G. & Hunter, D.H. 2015, *ApJ*, 805, 145
- Forbes, J.C., Krumholz, M.R., Burkert, A. & Dekel, A. 2014, *MNRAS*, 438, 1552
- Förster Schreiber, N. M., Genzel, R., Bouché, N., et al. 2009, *ApJ*, 706, 1364
- Fuhrmann, K. 1998, *A&A*, 338, 161
- Gilmore, G., & Reid, N. 1983, *MNRAS*, 202, 1025
- Hayden, M.R., Bovy, J., Holtzman, J.A., et al. 2015, *ApJ*, 808, 132
- Lee, Y.S., Beers, T.C., An, D., et al. 2011, *ApJ*, 738, 187
- Inoue, S. & Saitoh, T.R. 2014, *MNRAS*, 441, 243
- Kasparova, A.V.; Katkov, I.Yu., Chilingarian, I.V., Silchenko, O.K., Moiseev, A.V., & Borisov, S.B. 2016, *MNRAS*, 460, L89
- Kassin, S.A., Weiner, B.J., Faber, S.M., et al. 2012, *ApJ*, 758, 106
- Liu, C. & van de Ven, G. 2012, *MNRAS*, 425, 2144
- Lotz, J. M., Koekemoer, A., Coe, D. et al. 2017, *ApJ*, 837, 97
- Madau, P. 1995, *ApJ*, 441, 18
- Martig, M., Minchev, I., & Flynn, C. 2014, *MNRAS*, 443, 2452
- Merlin, E., Amorn, R., Castellano, M., et al. 2016, *A&A*, 590, A30
- Minchev, I., Martig, M., Streich, D., Scannapieco, C., de Jong, R.S., & Steinmetz, M 2015, *ApJ*, 804, L9
- Narayan, C.A., & Jog, C.J. 2002, *A&A*, 394, 89
- Pichon C., Pogosyan D., Kimm T., Slyz A., Devriendt J., Dubois Y. (2011) *MNRAS*, 418, 2493 1105.0210
- Robin, A. C., Reylé, C., Fliri, J., Czekaj, M., Robert, C. P., Martins, A.M.M. 2014, *A&A*, 569, A13
- Sánchez-Blázquez, P., Courty, S., Gibson, B.K., Brook, C.B. 2009, *MNRAS*, 398, 591
- Sandin, C. 2015, *A&A*, 577A, 106
- Stinson, G. S., Bovy, J., Rix, H.-W., Brook, C., Roskar, R., Dalcanton, J.J., Macciò, A. V., Wadsley, J., Couchman, H. M. P., Quinn, T. R. 2013, *MNRAS*, 436, 625
- Vera-Ciro, C., D’Onghia, E., Navarro, J., & Abadi, M. 2014, *ApJ*, 794, 173
- Vera-Ciro, C. D’Onghia, E., Navarro, J., & Abadi, M. 2016, *ApJ*, 833, 42
- Yoachim, P. & Dalcanton, J. J. 2006, *AJ*, 131, 226
- Yoachim, P. & Dalcanton, J.J. 2008a, *ApJ*, 682, 1004
- Yoachim, P. & Dalcanton, J. J. 2008b, *ApJ*, 683, 707